Article

Synergistic Effect of Pd Co-Catalyst and rGO–TiO₂ Hybrid Support for Enhanced Photoreforming of Oxygenates

Imran Majeed [1], Ayesha Arif [2], Afifa Idrees [2], Hafeez Ullah [1], Hassan Ali [1], Arshad Mehmood [3], Ashi Rashid [3], Muhammad Arif Nadeem [1] and Muhammad Amtiaz Nadeem [4,*,†]

1 Department of Chemistry, Quaid-i-Azam University, Islamabad 45320, Pakistan
2 Department of Chemistry, Government College University, Lahore 54000, Pakistan
3 Department of Chemistry, University of Engineering & Technology, Lahore 54000, Pakistan
4 Department of Environmental Sciences, Quaid-i-Azam University, Islamabad 45320, Pakistan
* Correspondence: manadeempk@gmail.com or nadeemmi@sabic.com
† Current address: SABIC-STC at KAUST, Thuwal 23955, Saudi Arabia.

Abstract: Photoreforming biomass-derived waste such as glycerol into hydrogen fuel is a renewable hydrogen generation technology that has the potential to become important due to unavoidable CO_2 production during methane steam reforming. Despite tremendous efforts, the challenge of developing highly active photocatalysts at a low cost still remains elusive. Here, we developed a novel photocatalyst with a hybrid support comprising reduced graphene oxide (rGO) and TiO₂ nanorods (TNR). rGO in the hybrid support not only performed as an excellent scavenger of electrons from the semiconductor conduction band due to its suitable electrochemical potential, but also acted as an electron transport highway to the metal co-catalyst, which otherwise is not possible by simply increasing metal loading due to the shadowing effect. A series of hybrid supports with different TNR and rGO ratios were prepared by the deposition method. Pd nanoparticles were deposited over hybrid support through the chemical reduction method. Pd/rGO-TNRs photocatalyst containing 4 wt.% rGO contents in the support and 1 wt.% nominal Pd loading demonstrated hydrogen production activity ~41 mmols $h^{-1}g^{-1}$, which is 4 and 40 times greater than benchmark Au/TiO₂ and pristine P25. The findings of this works provide a new strategy in optimizing charge extraction from TiO₂, which otherwise has remained impossible due to a fixed tradeoff between metal loading and the detrimental shadowing effect.

Keywords: reduced graphene oxide; TiO₂ nanorods; hydrogen; photoreforming; solar energy; palladium; electron transfer

1. Introduction

The current global economy is largely dependent on fossil fuels, which are virtually integral to industry, transport and everyday life. Massive global utilization of fossil fuels has caused critical and irreversible environmental problems throughout the world. Since fossil fuels are non-renewable, alternative energy sources are urgently needed to curb CO_2 emissions, which are considered as the main driver behind unpredictable climate changes. Among available fuels, hydrogen has been regarded as an excellent energy carrier due to its high energy content and zero emission of greenhouse gas [1]. Therefore, the research on advanced materials for technologies related to hydrogen production, as well as on hydrogen uptake, storage and delivery is becoming more important with each passing day. The development of efficient photocatalysts to produce hydrogen by water splitting using solar energy is an attractive environmentally friendly method, which offers a way to capture available solar energy and convert it into hydrogen [2]. However, pure water splitting is thermodynamically difficult and no major breakthrough has been achieved after decades of research [3–8]. At a power level of 1000 W/m^2, the solar energy reached on the earth's surface by far exceeds all human energy needs [9]. The amount of energy striking the Earth

from sunlight in one hour (4.3×10^{20} J) is more than the total energy consumed on this planet in one year (4.1×10^{20} J) [10]. Economic feasibility studies indicate that a 5% solar photon conversion to H_2 through the photoreforming of oxygenates would be competitive with conventional non-renewable processes (e.g., methane steam reforming) [11].

A broad spectrum of semiconductor materials has been explored for photochemical hydrogen production [12–14]. However, a few materials satisfy the basic requirements for effective photoreforming. These requirements include: (1) stability against photo-corrosion; (2) appropriate band positions and band gap (Eg); and (3) sufficient lifetime of charge carrier to deliver high H_2 production rates, because electron transfer reactions between semiconductor surfaces and organic molecules occur on microsecond timescales [15]. Considering the above requirements, TiO_2 is the most practical semiconductor photocatalyst for photoreforming, despite its drawbacks such as its rapid recombination rate of photoinduced electron (e^-) and hole (h^+), ability to make use of only 4% of available sunlight, low surface area and low charge carriers mobility [16,17]. In order to overcome these problem, many methods have been proposed to enhance its photocatalytic activity; the most effective of them are the deposition of high work function noble metals as co-catalysts, tailoring the semiconductor support [18] and the addition of hole scavengers [19]. The effect of metal, its amount and support type on the performance of the catalyst are summarized in Table 1. The amount of metal loading depends on multiple parameters, including type of metal, support and support surface area, and has been widely investigated. In most cases, the metal loading is below 5 wt.% metal loading [1,18,20–23].

The effect of the TiO_2 support on H_2 production rates in alcohol–water systems has been the subject of a number of investigations [18,19,24]. For example, H_2 production from alcohols in uniform, one-dimensional brookite TiO_2 nanorods is highly enhanced by engineering their length [25]. Deeper understanding of the roles of the TiO_2 support, i.e., crystallite size, surface area and TiO_2 phase composition may allow strategic and step-change improvements in M/TiO_2 photocatalyst design and performance. Rutile, a stable polymorph of TiO_2, generally has poor photocatalytic activity, owing to the fact that it is a direct band gap semiconductor, which allows fast electron–hole pair recombination following photoexcitation [26]. Anatase, a relatively less stable polymorph, is an indirect band gap semiconductor, typically displaying photocatalytic activities 1–2 orders of magnitude higher than rutile due to longer charge carrier lifetimes [27]. Mixed phase TiO_2 (P25) catalysts have also been widely studied, owing to synergistic electron transfer phenomena between the large proportion of Anatase phases and low proportion of rutile phases [28]. It appears that H_2 production using TiO_2-based catalysts has reached its plateau and there is only a marginal increase in rates. Further work needs to be focused more on fundamental understanding using state-of-the-art facilities that bring progressive improvements in capabilities. One-dimensional anatase TiO_2 nanostructures, including nanorods, nanotubes and nanofibers, which are produced hydrothermally, have favorable one-dimensional charge carriers transfer, improved reactant adsorption, reduced catalyst particle agglomeration in aqueous suspension, and lower e–h recombination [29]. Charge recombination is a critical problem that has, so far, limited the efficiency of photocatalysis. The holes are effectively confined to the width of the nanorods, whereas electrons are free to move over the whole length due to their 1D structure [30].

Recent studies of M/TiO_2 photocatalysts, where M = Pd, Pt, Au, Ag, Ni and Cu or combinations thereof, have reported H_2 production rates as high as 30–40 mmol $g^{-1}h^{-1}$ in alcohol–water systems under realistic solar UV fluxes [12,18]. Optimal metal co-catalyst loadings, 0.5−1.0 wt.% for Ni, Cu, Pd or Pt, and 1.5–4.0 wt.% for Au, largely depend upon the geometry of the semiconductor support. The photogenerated charge carriers separation in TiO_2 is achieved by the formation of rectifying the Schottky barrier established at the metal–semiconductor interface due to energy differences between the conduction band of the semiconductor and the work function of the metal [20,31–34]. The work functions of frequently used metals Pt, Pd, Au, Ni, Rh, Cu and Ag are 5.64, 5.12, 5.1, 4.98, 4.65 and 4.26 eV, respectively, and are larger than that of TiO_2 (4.2 eV). Platinum (Pt) is the most

frequently used metal to modify the TiO$_2$ photocatalyst surfaces because of its suitable work function [35], low overpotential for hydrogen evolution [36] and facilitation in the discharge of electrons from semiconductor nanoparticles into the electrolyte by forming an ohmic contact [37]. Major drawbacks of Pt used as a co-catalyst at TiO$_2$ for water splitting are its high cost and thermodynamically favorable back reaction of H$_2$ and O$_2$ at room temperature under atmospheric pressure [38,39]. According to some reports, complete photocatalytic decomposition of water is possible using Au, as compared with Pt, where the back reaction of H$_2$ and O$_2$ can be avoided on the former [40]. Cu and Ni have attracted much attention in recent years for hydrogen production due to the high synergism achieved when used in combination with each other [12,41,42]. Recently, Chen and coworkers achieved the highest hydrogen production activity (24.3 mmol h^{-1}g^{-1}) over Ni/TiO$_2$ by completely reducing the NiO over TiO$_2$ under a constant stream of 10% H$_2$ during calcination [43]. Cu is frequently deposited as Cu(OH)$_2$ over semiconductor supports to obtain metallic Cu by in situ reduction of Cu(OH)$_2$ during photoreactions [44,45].

Recently, palladium (Pd) has emerged as an efficient metal photocatalyst for water splitting [46–51]. The density of states in the vicinity of the Fermi level is higher for Pd than for Pt, Au and others, with the Fermi level of Pd being ∼0.2 eV higher than the Fermi level of Pt (−10.8 eV). Pd also has a much lower electron affinity and, hence, electron trapping capability, which may enable more facile electron transfer from Pd to protons for water reduction. Additionally, the high surface area offered by Pd due to the porous nature of metallic Pd may also contribute to its high activity [52]. It has been established by many authentic studies that Pd is more active than Pt and Au due to unique properties discussed later in this study [48,53]. Now, the whole focus is to prepare such a conductive semiconductor support for Pd co-catalyst that will help to improve the migration of photogenerated charge carriers to emerge at the surface. In this work, our group prepared a rGO−TiO$_2$ hybrid support and combined it with Pd metal co-catalysts for maximum hydrogen production. This system showed outstanding results due to the high synergism obtained by the high surface area of hybrid support and inherent electron scavenging properties of Pd metal.

2. Materials and Methods

All the reagents used were of analytical grade and used without further purification. Double distilled water was used in all the experiments. Commercially available Degussa P25 was obtained from Evonik Industries, Germany.

2.1. Synthesis of GO/TiO$_2$ Support

Sodium titanate (Na$_2$Ti$_3$O$_7$) nanorods were prepared by hydrothermal treatment of commercial TiO$_2$ (P25) powder according to the method reported elsewhere [54]. Briefly, TiO$_2$ (P25) powder (1 g) was dispersed in 10 M NaOH (50 mL). The white suspension obtained was sonicated for 15 min, stirred for 2 h and transferred into a 25 mL Teflon-lined stainless steel autoclave. The autoclave was then placed in a convection oven and heated at 150 °C for 48 h. The white precipitates of Na$_2$Ti$_3$O$_7$ thus obtained were collected by vacuum filtration and washed repeatedly with double distilled water until the pH of washing liquid was close to neutral. The Na$_2$Ti$_3$O$_7$ nanostructures were converted to hydrogen titanate (H$_2$Ti$_3$O$_7$) nanostructures by ion exchange method by suspending the former in 0.1 M HCl (500 mL) for 1 h. The H$_2$Ti$_3$O$_7$ nanostructures were collected by vacuum filtration, washed with double distilled water until the washing liquid was neutral to pH paper and finally dried at 80 °C for 12 h. The highly crystalline TiO$_2$ nanorods (TNRs) were obtained in air by calcining H$_2$Ti$_3$O$_7$ nanostructures at 400 °C for 2 h.

Graphene oxide (GO) was synthesized by modified Hummers method [55]. Finally, a hybrid photocatalyst support GO–TNR with high surface area was synthesized through simple deposition method. Briefly, a known amount of graphene was suspend in 30 mL ethanol water mixture (1:1) and sonicated for 2 h. TNRs (200 mg) were added into the above slurry, sonicated for 30 min and then finally stirred for 1 h, which resulted in a

homogenous blackish mixture. The GO–TNR hybrid support was recovered through vacuum filtration, washed several times with distilled water and dried in air at 100 °C. GO/TNR with 1–4 wt.% GO loading were obtained.

2.2. Metal Co-Catalyst Loading

Pt, Pd and Au were loaded through surfactant-assisted $NaBH_4$ reduction method. Briefly, 250 mg of GO–TNR was added into 30 mL of distilled water in a flask and stirred for 1 h to make a homogeneous slurry. A Polyvinlyalcohol (PVA) solution (PVA/metal = 2:1) was prepared in 20 mL of distilled water at 100 °C in a separate beaker. Metal ions were encapsulated by adding PVA solution to required amount of metal solution and stirred for a further 1 h. Later, metal solution was added to the GO–TNR slurry drop wise with vigorous stirring. The metal ions were reduced and deposited on GO–TNR during the slow addition of $NaBH_4$ solution (metal/$NaBH_4$ = 1:10) under continuous stirring. The slurry was stirred for a further 5 h, precipitates were vacuum filtered, washed two times with distilled water and dried in oven at 80 °C for 16 h. Characterization results (shown later) confirmed that $NaBH_4$ addition not only deposits metal on the hybrid support, it also reduces graphene oxide (rGO). The final photocatalyst powders with 1 wt.% Pd and 1–4 wt.% rGO were obtained by calcining the powder at 350 °C for 5 h. The subscript in the photocatalyst indicates wt.% loading. The Pd metal loading was confirmed by inductively coupled plasma optical emission spectrometry (ICP-OES) using a PerkinElmer (Optima 8300) spectrometer.

2.3. Hydrogen Production Experiments

Photocatalytic hydrogen production tests were conducted in a Pyrex reactor (140 mL). Initial tests were conducted by changing catalyst amounts in a 1–20 mg range and the maximum H_2 production rate was obtained with 2.5 mg in the reactor containing 25 mL of an aqueous alcohol–water mixture (20 vol.% ethanol or 5 vol.% glycerol). The factors effecting optimal loading are discussed elsewhere [44,56]. Prior to the start of each photocatalytic experiment, the reactor was continuously bubbled with nitrogen at a flow rate of 10 mL min^{-1} for 30 min to remove dissolved and headspace oxygen. Molecular oxygen can trap electrons from the TiO_2 conduction band to produce superoxide radicals, which can subsequently mineralize organic sacrificial agents [57]. A Spectroline model SB-100P/F lamp (100 W, 365 nm) at a distance of 10 cm from the reactor was used for UV light excitation of the photocatalysts. The photon flux measured at the sample was ~6.5 mW cm^{-2} (comparable to UV flux in sunlight). Hydrogen generation was monitored by taking head space gas samples (0.5 mL) at regular time intervals with a gas tight syringe and injecting them into a gas chromatograph (Shimadzu GC 2014) equipped with a TCD detector and molecular sieve capillary column (length = 25 m; ID = 0.32 mm; average thickness 0.50 μm). H_2 produced through photoreaction was quantified against an internal calibration curve. The photocatalytic tests for each sample were repeated at least three times for accuracy. To assess the catalyst's stability, four consecutive hydrogen production tests were carried out, where each test lasted for four hours, for the most active Pd_1/rGO_4TNRs catalysts using a 5% glycerol–water mixture. The catalyst was filtered, dried and added to the fresh 5% glycerol–water mixture each time before starting the subsequent test.

2.4. Photocatalysts' Characterization

Powder XRD patterns were collected with a Siemens D−5000 Diffractometer equipped with a curved graphite filter monochromator. XRD data were collected over the 2θ range 10–70θ (step size 0.058, scan rate 2° min^{-1}) by using CuK$_\alpha$ X-rays (l = 1.5418 A, 40 mA, 40 kV). XRD confirmed that TNR were made up of anatase phases. TNR crystallite size (L) was determined using the Scherer equation (L = 0.9λ/βcosθ) and line-widths of the anatase (101) reflection at 2θ = 25.38. UV/Vis absorbance spectra were collected over the wavelength range 200–900 nm with a Thermo Fisher Scientific UV/Vis spectrophotometer equipped with a praying mantis diffuse reflectance accessory. The Brunauer–Emmett–Teller

(BET) method was used to measure the surface area of all the samples. TEM analyses were performed by using a Philips CM12/STEM Electron Microscope, PW 6030 (120 kV). XPS data were collected by using a Kratos Axis UltraDLD equipped with a hemispherical electron energy analyzer and an analysis chamber at base pressure ~1×10^9 Torr. Samples were excited by using monochromatic AlKα X-rays (1486.69 eV) with the X-ray source operating at 150 W. Samples were gently pressed into ~0.1 mm thick pellets for the analyses. A charge neutralization system was used to alleviate sample charge build up during analysis. Survey scans were collected at a pass energy of 80 eV over the binding energy range 1200–0 eV, whereas core level scans were collected with a pass energy of 20 eV. The spectra were calibrated against the C1s signal at 284.80 eV from adventitious hydrocarbons. Steady-state and time resolved photoluminescence (PL) measurements were carried out using a Flau Time 300 (FT-300) steady-state and lifetime spectrometer, PicoQuant GmbH, Berlin, Germany. The PL was measured using a pulsed LED laser excitation source, PLS-300, centered at 305 nm with a full-width half-maximum (FWHM) of ~416 ps and pulse energy 0.077 pJ. The PL curves were fitted using Easy Tau (Version 2.2, PicoQuant, GmbH Berlin, Germany) and FluoFit (Version 3.3, PicoQuant, GmbH Berlin, Germany) software. The electrochemical experiments were performed using an SP-300, Bio-Logic Potentiostate with three electrode system, catalyst ink impregnated glassy carbon (GCE) as the working electrode, platinum wire as an auxiliary electrode (counter) and Ag/AgCl as reference electrode and with 0.1 M aqueous Na_2SO_3 as the electrolyte. Electrochemical impedance spectroscopy (EIS) experiments were carried out in the frequency range of 1.0 MHz to 1.0 Hz with amplitude of 10 mV at 200 mV potential (vs. Ag/AgCl). We did not characterize the recovered catalysts due to no observable change in the catalyst activity. In general, metal-supported TiO_2 photocatalysts remained stable during photoreactions due to the stability of TiO_2 itself, as well as metal in a reducing environment. In the case of non-oxide semiconductors, for example, CdS, we have reported significant changes [58,59].

3. Results and Discussion

3.1. Characterization

Inductively coupled plasma optical emission spectrometry (ICP-OES) confirmed that the Pd loading was similar to its initial nominal loading. The Brunauer–Emmett–Teller (BET) surface areas for P25 and TNR were found to be 49 and 62 m^2 g^{-1}, similar to the literature values. The metal loading did not change the surface area. Figure 1a, the UV-visible diffuse reflectance spectroscopy (DRS), shows that TNR absorbs strongly in the UV region up to 380 nm, and after that there is sharp decrease in the absorbance edge and no significant absorbance in the visible region. rGO shows absorbance through the UV up to the visible region. After depositing Pd on the TNR, the absorbance edge is clearly extended into the visible region, indicating Pd deposition over support. This extension in absorption has been attributed to a combination of metal d−d transitions and formation of −O−Pd−O− species at the TNRs' surface [53]. When Pd is deposited over rGO/TNR composites, the absorbance by palladium is conspicuously dominated by graphene, and there are new absorption features in the absorption spectra, a solid evidence of strong electronic synergism among loaded Pd and TNRs−graphene hybrid support. The strong absorption in the visible region is attributed to the black color and formation of the Ti−O−C bond in the hybrid support [60]. With the increase in rGO content over TNRs, the absorbance is further increased. The UV-visible diffuse reflectance spectroscopy of rGO-TNRs and Pd/rGO looks exactly like Pd/rGO-TNRs and rGO alone, respectively.

Figure 1b, the XRD pattern of rGO, exhibits a typical broad peak at 2θ = 25° (hkl = 002), which is ascribed to disordered stacks of weakly crystalline rGO nanosheets [61]. The hydrothermally prepared TNRs calcined at 400 °C show all peaks of anatase phase. The XRD pattern of the most active photocatalysts Pd_1/rGO_4−TNRs showed no obvious peak of Pd due to their low concentration and high dispersion. The diffraction peak of rGO is suppressed by a strong peak of anatase (101) in the region between 2θ = 25–30°. If we

closely observe this region, the anatase (101) peak is clearly widened at the base, implying the presence of rGO.
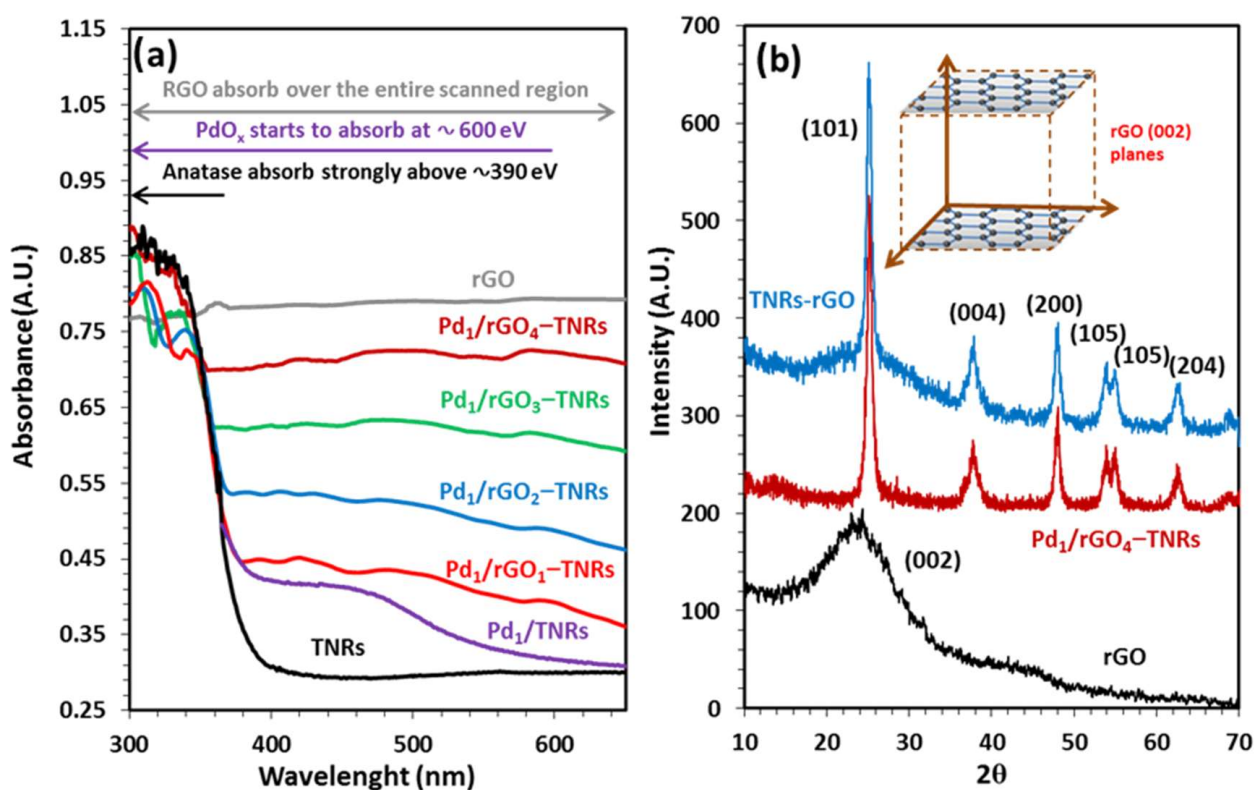
Figure 1. (**a**) Diffused reflectance UV-Visible spectra of as prepared TNR, rGO, Pd_1/TNRs and Pd_x/rGO_x−TNRs with different compositions. (**b**) Powder XRD patterns of as prepared rGO, TNRs and Pd_1/rGO_4−TNRs.

Figure 2a, the FTIR spectrum of rGO, is characterized by a strong and relatively broad carbonyl peak at 1720 cm^{-1}, accompanied by an aromatic C=peak at 1618 cm^{-1}, confirming the formation of rGO and the presence of sp^2, as well as sp^3 carbon atoms [51,62]. The broad absorption peak between 3000 and 3500 cm^{-1} is due to the acidic −OH and moisture content. The Raman spectrum of rGO in Figure 2b clearly shows the D band at 1337 cm^{-1} and G bands at 1571 cm^{-1}. The D band is due to the disorder present in the graphitic plane (sp^3 defects and disorders) and the G band refers to the presence of in-plane vibrations of sp^2 carbon atoms in rGO [63,64]. Raman spectra of Pd_1/rGO_4 catalyst shows that the peak intensity of D band is decreased as compared with pristine rGO, due to the reduction of rGO by the addition of $NaBH_4$, which decreased the disorder in the graphitic planes. A slight shift observed in the D band, higher D band to G band intensity ratio and overall lower intensity is due to the presence of TNR.

Figure 3 shows the C 1s XPS spectra for Pd_1/rGO_4−TNR. After deconvolution, it is clearly evident that the C1s spectrum contains seven peaks at 282.7, 284.5, 285, 286.5, 288, 289 and 290.9 eV, corresponding to the carbidic carbon (C≡C)$^{2-}$ as well as carbon bonded to Pd, sp^2 carbon (C=C), sp^3 carbon (C-C, C-H), hydroxyl carbon (C-OH, C-O-C), carbonyl carbon (C=O), carboxyl carbon (O-C=O) and π→π* satellites, respectively [65]. A peak area ratio of more than five between sp^2 carbon and hydroxyl carbon indicates the presence of graphene in its reduced state [66]. Palladium is found to present as Pd and PdO. Given the fact that Pd is reduced very easily under X-rays, it is most likely that it is mainly present as PdO. This leads to the main reason behind the induction period observed during the photoreforming reaction where PdO was converted into Pd metal to reach steady state rates. We did not present Ti3d and O1s spectra, as they were similar to what has been

reported elsewhere and did not carry any additional information [12,18,42,67,68]. Figure 4a shows highly dispersed and well-shaped TNR with length ca. 50–70 nm. Figure 4b shows rGO nanosheets that are folded at the edges and Pd nanoparticles of an average particle size of 2–5 nm, which are uniformly distributed over the rGO sheets with no agglomerates. After blending rGO with TNRs, Pd structural features are not clearly seen due to very low loading amounts (4 wt.%). Figure 4c shows the hybrid nano-composites in which TiO_2 nanorods are clearly interconnected by the rGO sheets. This type of hybrid structure is highly beneficial for vectorial charge transfer from TiO_2 to catalytically active metal sites for proton reduction and enhancing the photocatalytic efficiency [69]. The intimate contacts in the heterojunction of three components, i.e., TNRs, rGO and Pd particles are clearly noted in Figure 4d.
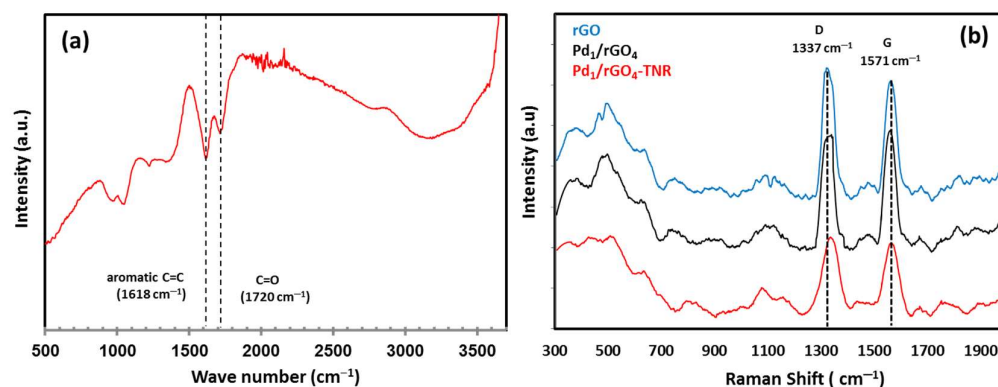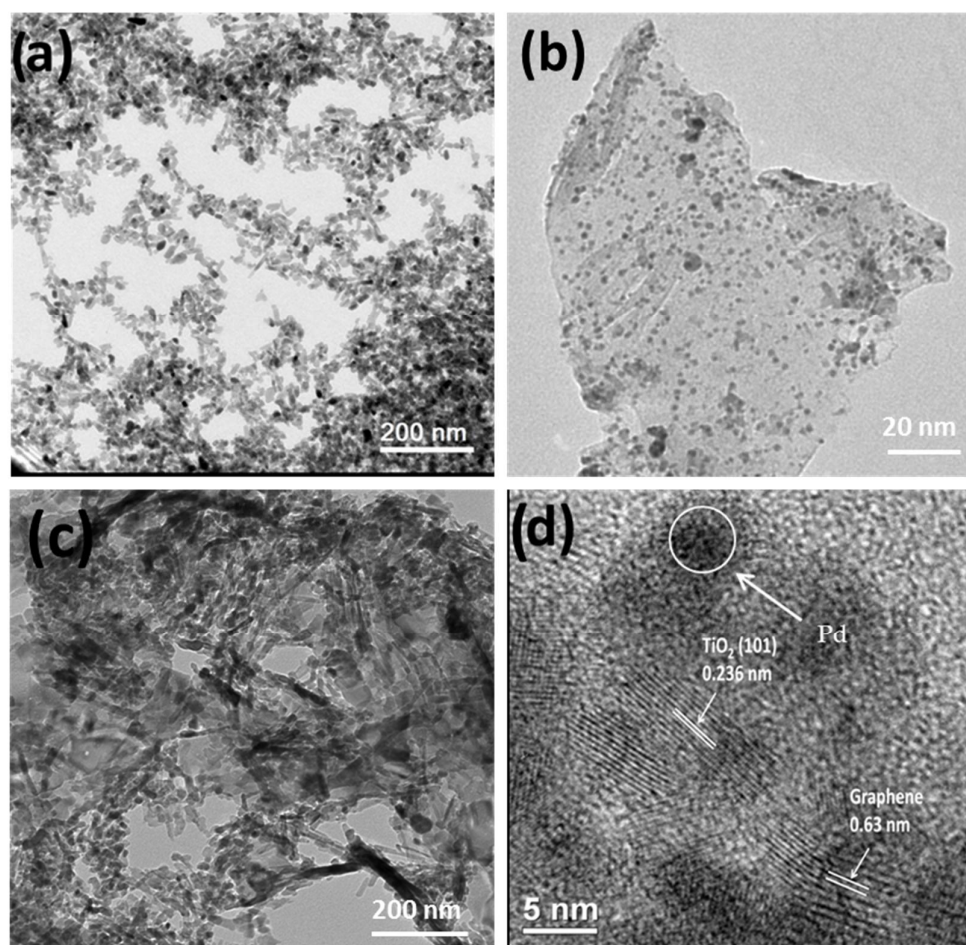

Figure 2. (**a**) FTIR spectrum of pristine rGO. (**b**) Raman spectra of pristine rGO, Pd_1/rGO_4 and Pd_1/rGO_4-TNR.
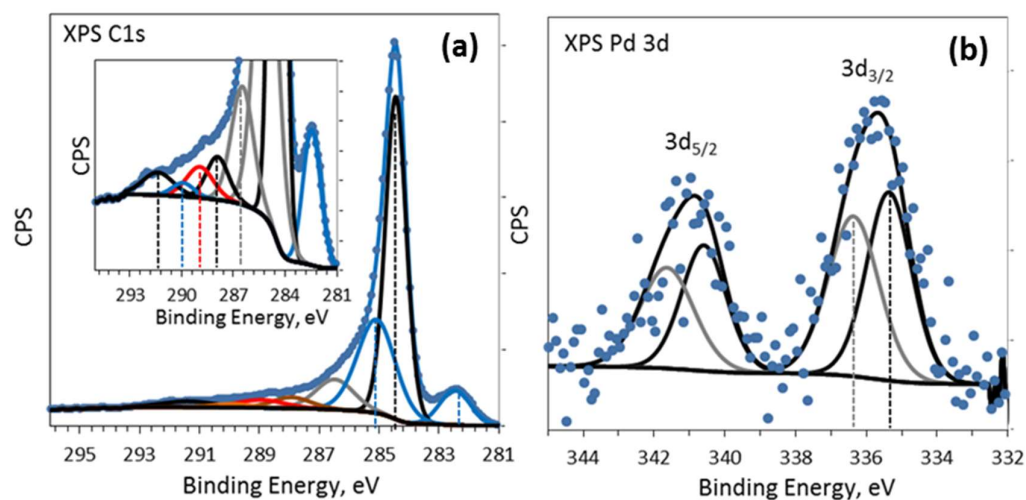
Figure 3. XPS C1s (**a**) and XPS Pd3d (**b**) spectra of Pd_1/rGO_4-TNR. The inset in (**a**) is a rescaled (**a**) to clearly show XPS C1s peaks with a relatively lower intensity.

Figure 4. Transmission electron microscopy (TEM) images of pristine TNRs (**a**), Pd_1-rGO (**b**) and Pd_1/rGO_4-TNR (**c**,**d**).

To probe into the electron transfer, kinetics photoluminescence (PL) experiments were performed with as prepared materials as well as benchmark metal co-catalysts (Pt and Au)-loaded TNRs. Charge carriers' recombination in TNRs is expected to be suppressed by deposition of Pt, Pd and Au due to the transfer of photo-excited electrons from the conduction band of TNRs to metal nanoparticles. In Figure 5a, pristine TNRs give intense photoluminescence signal due to the recombination of excited electrons with holes following photoexcitation under 310 nm. Metal co-catalyst loading strongly attenuates the photoluminescence signal of TNRs, with the extent of attenuation following the order $Pt/TNRs > Au/TNRs \approx Pd/TNRs > Pd_1/rGO_4-TNRs$. These data show that each metal center is acting as a good electron acceptor, and thus increasing the lifetime of charge carriers available for photoreactions. Importantly when rGO was deposited over TNRs with the Pd, the intensity of the PL signal decreased many folds, which indicates rGO as an excellent conduction band electrons sink as compared with all metals. A similar kind of effect was noted when Pt and Au were deposited along rGO over TNRs, indicating the electron-accepting ability of rGO dominates metals co-catalysts. Conversely, Pt exhibited lower PL intensity than Pd and Au, in line with its superior activity for hydrogen production than other metals. The EPR results of other researchers have indicated that Pt is more efficient than Au in facilitating such charge transfer from Ti^{3+} to M [70]. Electrochemical impedance spectroscopy (EIS) was performed to study the interfacial charge transfer. The Nyquist plots of TNRs, $Pd_1/TNRs$, $Pt_1/TNRs$, $Au_1/TNRs$ and Pd/rGO_4-TNRs are shown in Figure 4b. In general, a smaller arc radius size indicates lower charge transfer resistance. Among all materials, Pd/rGO_4-TNRs shows the smallest arc radius, indicating that it offers the lowest resistance/highest mobility to interfacial charge transfer. Pd/TNR and

Au/TNRs show a similar ability to charge transfer, whereas Pt shows the best charge transfer ability among the three metals. This charge transfer trend of Pt, Pd and Au is directly related to their work functions (5.7, 5.6 and 5.3, respectively) [71]. The arc radius is largest for the pristine TNRs reflecting the lowest charge mobility
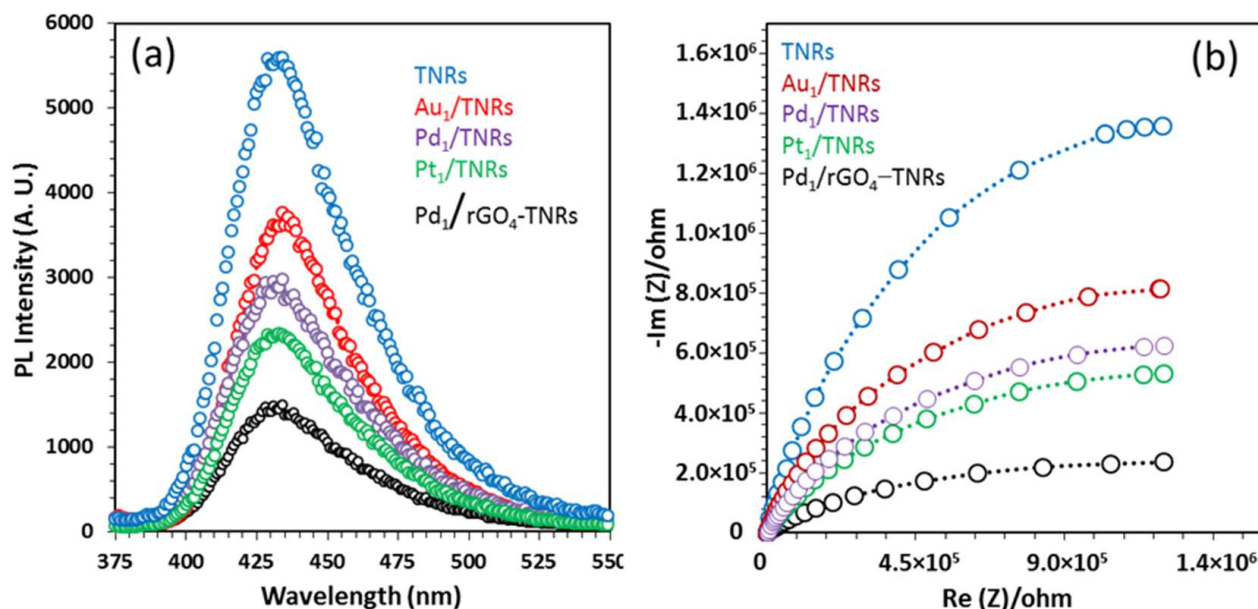

Figure 5. (**a**) Steady-state photoluminescence (PL) measurements and (**b**) EIS Nyquist plots of pristine TNRs, $Pd_1/TNRs$, $Pt_1/TNRs$, $Au_1/TNRs$ and Pd_1/rGO_4-TNRs.

3.2. Photoreforming Activity

The hydrogen production rates of different materials were recorded in 5 vol.% glycerol−water mixtures under UV flux of intensity ~6.5 mW cm^{-2} (comparable to UV flux in sunlight). Figure 6a shows that once the induction period has elapsed, a constant rate of reaction is observed (inset Figure 6a). As observed in XPS analysis, this induction period is related to PdO reduction to Pd [56,67]. It is to be noted that pristine TNR does not show any induction period. In Figure 6b, the pristine TNRs show very low rates of hydrogen production (2.2 mmol h^{-1}g^{-1}) due to the higher recombination rates of photogenerated charge carriers. After the introduction of 1 wt.% of Pd, the H$_2$ production rate rapidly increased to 26.33 mmol h^{-1}g^{-1} as the Pd metal suppressed the charge carriers' recombination by scavenging the conduction band electrons and acted as a cathodic reduction/recombination site for protons. The addition of layered rGO with TNRs support resulted in a significant improvement of hydrogen production activity, and the content of rGO in TNRs had a significant influence in this unique hybrid combination. In the presence of rGO (1.0 wt.%) in the hybrid support, the activity was enhanced to 30.66 mmol h^{-1}g^{-1}. The hydrogen production rate gradually increased with the increase in rGO contents, and the highest value was achieved at 4 wt.% (41 mmol h^{-1}g^{-1}); after that, the rate started to decrease due to the shadowing effect on support (discussed later).

Figure 7a explains the effect of the overall Pd loading amount over TNRs. The highest rate of hydrogen production was achieved over TNRs at an overall nominal metal loading amount of 1 wt.%. Recent studies proved that 0.5 wt.% Pd loading over P25 nanoparticles showed the maximum rate of hydrogen production [13]. At the same time, both 1 and 0.5 wt.% Pd/P25 showed less activity than 1 wt.% on Pd/TNRs. The reason behind the superior activities of TNRs compared with P25 is ascribed to their excellent charge transportation and longer e$^-$/h$^+$ lifetime due to following features: 1. effective vectorial transfer of photogenerated charges due to a nanorod structure; 2. the charge carriers can not only move easily along the longitudinal direction, but they also have to travel short distances to emerge at the surface transversely; 3. lower number of surface defects, thus a small number of recombination sites; 4. TNRs support possesses high surface area

$(62\ m^2g^{-1})$ compared with P25 $(49\ m^2g^{-1})$, and a greater proportion of reactive anatase surface facets, such as anatase (101), as seen in Figure 4d, though further HRTEM studies are needed to establish the nature of all the anatase facets exposed by the TNRs support [54]. A slight decrease in hydrogen production activity at 1.2 wt.% Pd loading over TNRs was observed, and after that there was a gradual decrease in activity up to 2 wt.% loading. This decrease in activity with an increased amount of metal loading has also been observed by others [18]. It has been suggested that metal particle size, increased surface defect concentration and shadowing of incoming light by metal nanoparticles might be behind this. To clarify this, a systematic study using slurry phase reactions as well as model surfaces is required. A lower amount of hydrogen production was also observed at 0.5 wt.% Pd loading. This is due to the availability of fewer active metal sites over TNRs for proton reduction or hydrogen recombination. As a consequence, a suitable content of Pd is crucial for the optimized photocatalytic performance of Pd/rGO−TNRs photocatalysts.
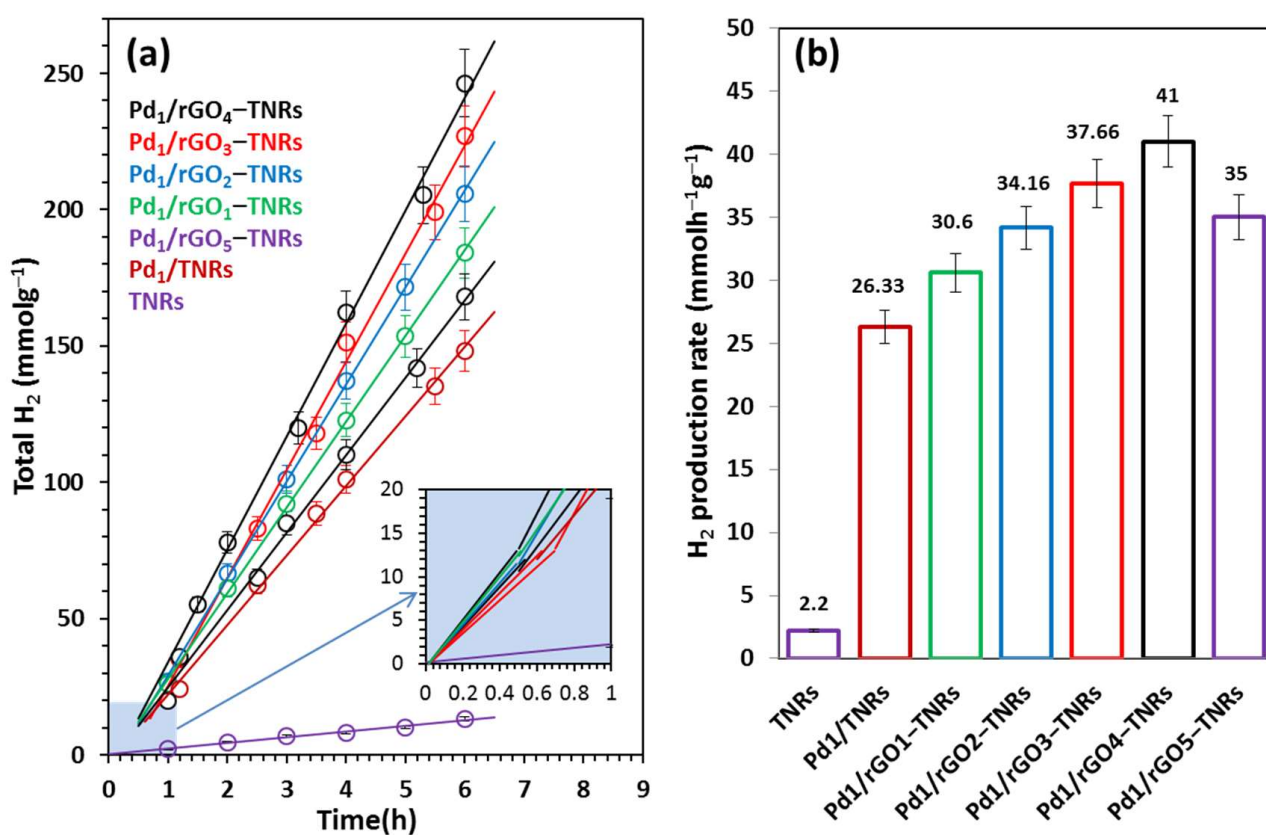
Figure 6. Comparison of H_2 production over TNRs, Pd_1/TNRs, Pd_1/rGO_1−TNRs, Pd_1/rGO_2−TNRs, Pd_1/rGO_3−TNRs, Pd_1/rGO_4−TNRs and Pd_1/rGO_4−TNRs photocatalysts in 5 vol% glycerol/water mixtures. (**a**) and (**b**) show the total amount of H_2 production as a function of time and H_2 production rates for different catalysts, respectively. The inset in (**a**) highlights the induction period.

Figure 7b shows the comparison between three benchmark co-catalyst (Pt, Pd, Au) loaded TNRs and Pd_1/rGO_4−TNRs photocatalysts in the current study. In 5 wt.% glycerol–water system, 1 wt.% Pd/TNRs demonstrated superior hydrogen production than the other two [13]. Under present conditions, the order of activity was observed as Pd > Pt > Au. It has been established that metal co-catalyst particle size has no considerable effect on the photo-catalytic activity, so the key factor to consider might be the work function of Pd, Pt, Au and TNRs (5.7, 5.2, 5.1 and 4.26) [50]. Theoretically, Pt should be more active when compared with Pd and Au due to the larger height of the Schottky barrier and other intrinsic catalytic properties. The main reason behind this might be the favorable thermal back

reaction of O_2 and H_2 to form water. Recently, palladium (Pd) has emerged as an efficient metal co-catalyst compared with Au and Pt in water splitting because the density of states in the vicinity of the Fermi level is higher for Pd than that for Pt and Au, with the Fermi level of Pd being ~0.2 eV higher than the Fermi level of Pt (−10.8 eV) [13,46,48,49]. Pd also has a much lower electron affinity and, hence, electron trapping capability, which may enable more facile electron transfer from Pd to proton for water reduction [47]. Su and co-workers probed the kinetics of the photogenerated electrons on metal semiconductor photocatalyst systems and found that a fast proton reduction occurs on Pd/TiO$_2$ as compared with Au/TiO$_2$. It was revealed that Pd shows a slow reverse transfer process of electrons from metal to TiO$_2$ (low k_{rev}) for the trapped photogenerated electrons. Pd most likely provides an ohmic contact, whereas Au shows capacitive properties [72]. Additionally, the high surface area offered by Pd due to the porous nature of metallic Pd may also contribute to its high activity [52]. The combination of the above factors is likely the reason behind the selection of Pd for further experiments with highly efficient hybrid rGO−TNRs support. Moreover, Pd co-catalyst was also loaded over Anatase TiO$_2$ nanoparticles prepared by sol-gel (SG) and hydrothermal (HT) techniques. Pd$_1$/rGO$_4$−TNRs photocatalyst showed superior hydrogen production activity than both Pd/SG (anatase) and Pd/HT (anatase) due to the high synergism achieved by efficient hybrid organic−inorganic support and the inherent catalytic properties of Pd metal. From Table 1, it can be noted that the unique photocatalyst developed in this study gives far better hydrogen production rates as compared with catalysts reported in the literature.
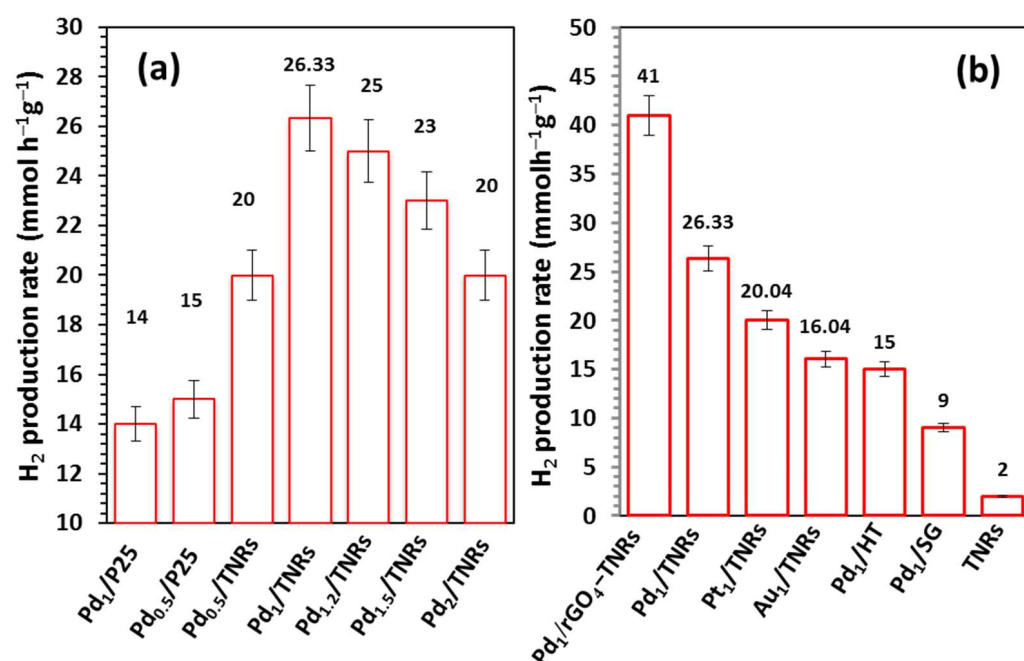
Figure 7. (**a**) Metal co-catalyst loading optimization on TNR and benchmark P25 and its effect on amount of H$_2$ production in 5 vol.% glycerol–water mixtures. (**b**) Comparison of Pd$_1$/rGO$_4$−TNRs with other benchmark photocatalysts prepared with different supports.

Table 1. Comparison of hydrogen production rates on metal-supported TiO_2 catalysts. The subscripts with metal and graphene indicate their wt.% with respect to oxide support. (A = anatase; R = rutile; NR = nanorods; NS = nanosheets; NF = nanofibers).

Photocatalyst Structure	Sacrificial Reagents	Irradiation	H_2 Production $(mmol\ g^{-1}h^{-1})$	Ref.
$Pd_1-rGO_4/TNRs$	5% glycerol–water	100 W (UV)	41.0	Present Study
$Cu_{0.8}$-$Ni_{0.2}/TNR_{130}$-400	5% glycerol–water	100 W (UV)	35.1	2017 [18]
$Pt_{0.5}-rGO_{0.5}/P25$	30% methanol–water	300 W(UV)	0.750	2012 [73]
$Pt_{0.5}-rGO_1/TiO_2$-A (NS)	25% methanol–water	350 W (UV)	0.736	2011 [74]
$rGO(sheets)_2/P25$ (NR)	Na_2S and M Na_2SO_3	500 W (UV)	0.054	2012 [75]
rGO_5/TiO_2-A	Na_2S and Na_2SO_3	(UV)	0.085	2010 [76]
$rGO_{20}/P25$	20% ethanol–water	200 W (UV)	0.74	2011 [60]
$Pt_{0.05}-Graphen_{0.7}/P25$	10% methanol–water	300 W(UV)	0.1	2012 [77]
$MoS_2(0.5)/GO_{0.5}-TiO_2$-A	25% ethanol–water	300 W (UV)	2.06	2012 [69]
GO/CuO_2-P25	10% methanol–water	500 W (UV)	2.9	2013 [78]
$CuO_{1.25}/TiO_2$	80% ethanol–water	100 W (UV)	20.3	2013 [79]
$Ni(OH)_{(0.5)}/P25$	25% methanol–water	3 W (UV)	3.056	2011 [80]
$Ni_{1.25}/P25$	95% ethanol–water	100 W (UV)	20.7	2015 [19]
$Ni(OH)_{2(0.5)}/P25$	25% methanol–water	3 W (UV)	3.056	2011 [80]
$Au_4/P25$	5% ethanol–water	450 W (UV-Vis)	6.12	2013 [81]
$Au_{0.8}/TiO_2$-A	25% methanol–water	400 W (UV)	1.54	2014 [82]
Au_1/TiO_2-A	6% methanol–water	250 W (UV-Vis)	8	2008 [83]
Au_1/TiO_2-A	50% methanol–water	2.4 W (UV)	8.4	2012 [84]
$Au_{0.5}$-$Pt_{0.5}/TiO_2$-A	50% ethanol–water	125 W (UV)	8	2013 [85]
Pd_1/TiO_2-A+R (NS)	50% ethanol–water	8 W UV-B	16.2	2015 [86]
$Au_{1.5}/P25$	80% ethanol–water	100 W (UV)	32.2	2015 [54]
$Au_{0.25}$-$Pd_{0.75}/P25$	25% glycerol–water	100 W (UV)	19.6	2014 [72]
$Pt_1/P25$	10% glycerol–water	200 W (UV)	27.1	2015 [13]
$NiO_{(2)}/TiO_2$-A+ R	16% glycerol–water	500 W (UV)	1.23	2016 [87]

Table 2 summarizes structural, chemical composition and hydrogen evolution data for different photocatalysts and shows that Pd_1/rGO_4-TNRs is the most active among all the tested catalysts. The stability of photocatalytic systems is a crucial issue that requires adequate understanding. Long-term performance needs to be assessed even though no one has reported any stability issue. Since strongly reducing conditions preserves the metal in its metallic state and keeps it stable under photoreaction conditions, it is commonly accepted that non-Nobel metals are stable systems [42,88]. The stability and reactivity of the Pd_1/rGO_4-TNRs photocatalyst was checked by consecutive runs for a total time period of 16 h without any sign of deactivation, as shown in Figure 8. A considerable increase in rate was observed for the second and third runs and a rate of 46 mmol $g^{-1}h^{-1}$ was achieved. This indicates a very high stability and activity of our best performing photocatalyst with time. Ongoing from the third to fourth run, a slight decrease in line slope was observed due to the deposition of photocatalyst particles (clearly seen with the naked eye) on the reactor walls with time, thus scattering away a small fraction of incoming light radiation, and also potentially due to the decrease in the sacrificial reagent.

Table 2. Summarized structural, chemical composition and hydrogen evolution data for different photocatalysts.

Photocatalyst	BET Surface Area ($m^2 \, g^{-1}$)	TNR Length (nm)	rGO Nominal (wt.%)	Pd wt.% by XPS	H_2 Production (mmol $h^{-1} g^{-1}$)
TNR	60.45	50–70	–	–	2.00
$Pd_1-rGO_1/TNRs(TiO_2)$	60.25	50–70	1	–	30.60
$Pd_1-rGO_2/TNRs(TiO_2)$	61.05	50–70	2	–	34.16
$Pd_1-rGO_3/TNRs(TiO_2)$	61.75	50–70	3	–	37.66
$Pd_1-rGO_4/TNRs(TiO_2)$	62	50–70	4	0.85	41.00
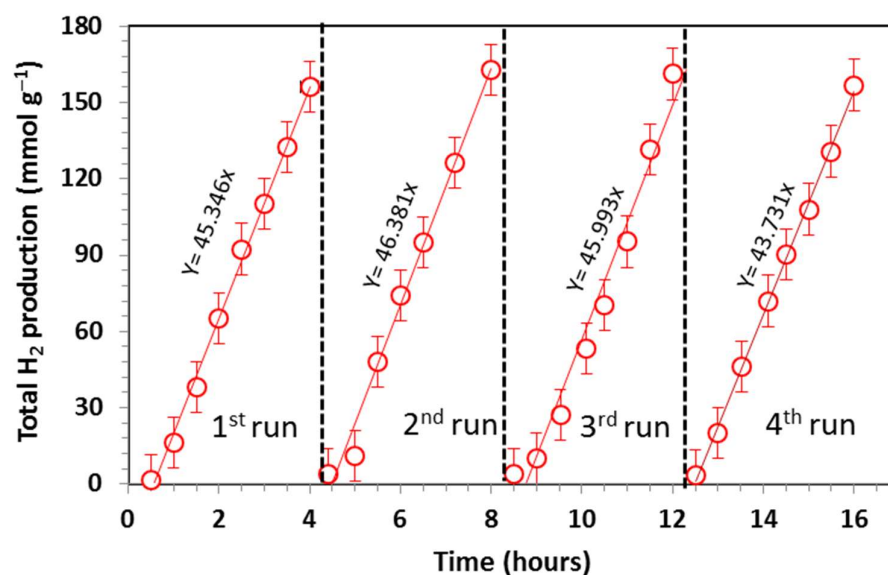
Figure 8. Consecutive runs for the hydrogen generation tests with Pd_1/rGO_4-TNRs catalysts using 5% glycerol−water mixtures.
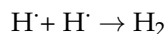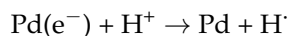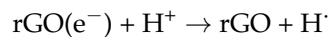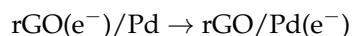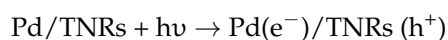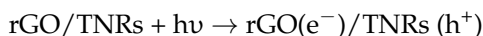
3.3. Hydrogen Production Mechanism

Based on the characterization, unique optical and charge transfer properties of hybrid support and efficient hydrogen production activities on the $Pd_1-rGO_4/TNRs$ photocatalyst, a possible hydrogen production mechanism is proposed and is illustrated in Figure 9. Upon irradiation, e^-/h^+ pairs are generated in the TNRs; however, these photoinduced e^-/h^+ pairs are likely to recombine if not quenched efficiently. We loaded inorganic support (TNRs) with highly conductive rGO, which not only quenched the electron from the conduction band of TNRs but also acted as an efficient electron transport highway to Pd nanoparticles. Secondly, Pd nanoparticles quenched the electrons directly from the conduction band of TNRs and also received the charge through highly conductive rGO sheets. Previous studies have shown that the CB electrons of TiO_2 can be injected into the rGO sheets because the redox potential of rGO is slightly lower than the CB of anatase TiO_2 [69]. The mobility of these electrons on the graphene sheets is very high. Thus, rGO greatly enhanced the charge separation and provided additional sites for proton reduction/recombination along with Pd metal.
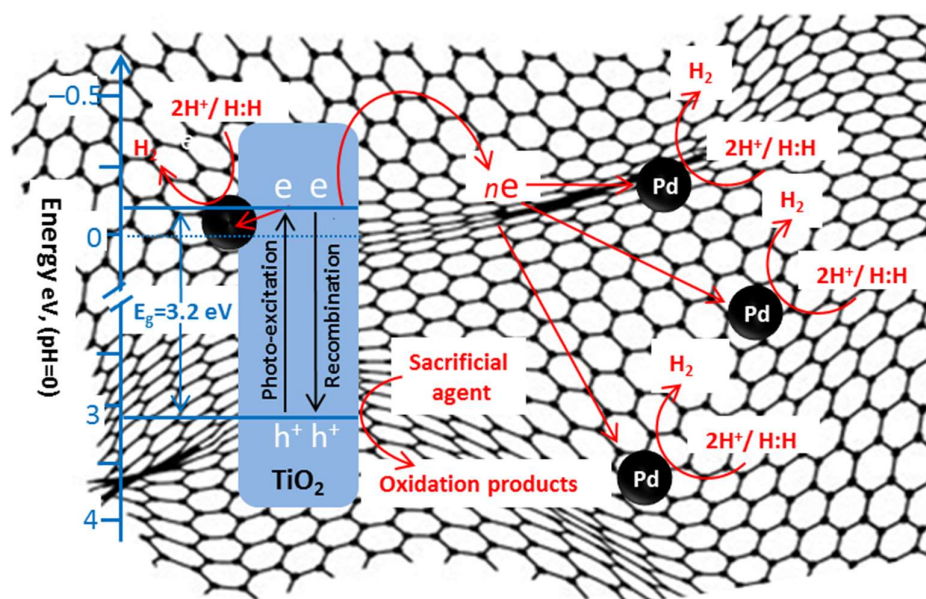
Figure 9. Photocatalytic hydrogen production over Pd_1/rGO_4-TNRs photocatalysts.

The whole mechanism can be represented as;

$$rGO/TNRs + h\upsilon \rightarrow rGO(e^-)/TNRs\ (h^+)$$

$$Pd/TNRs + h\upsilon \rightarrow Pd(e^-)/TNRs\ (h^+)$$

$$rGO(e^-)/Pd \rightarrow rGO/Pd(e^-)$$

$$rGO(e^-) + H^+ \rightarrow rGO + H^{\cdot}$$

$$Pd(e^-) + H^+ \rightarrow Pd + H^{\cdot}$$

$$H^{\cdot} + H^{\cdot} \rightarrow H_2$$

4. Conclusions

The photocatalytic activity depends upon photogenerated charge carriers scavenging from the semiconductor support at the nano- to picoseconds time scale. To achieve this, an inorganic–organic hybrid support containing TiO_2 nanorods blended with an extraordinary conductive graphene oxide was fabricated. This support showed a great potential to transport charge carriers to loaded metal. rGO present in support performed a dual function, including effective electron quenching from the conduction band of TiO_2 nanorods and working as a highly conductive electron pathway for Pd nanoparticles deposited over support. Pd_1/rGO_4-TNRs photocatalyst containing 4 wt.% rGO contents in the support and 1 wt.% nominal Pd loading demonstrated excellent hydrogen production activity ~41 mmols $h^{-1}g^{-1}$, which is 4 and 40 times greater than benchmark Au/TiO_2 and pristine P25. This study demonstrates that highly conductive rGO can be used to effectively enhance photoreforming reaction rates by allowing additional mechanisms for electron transfer between TiO_2 and organic adsorbates.

Data Availability Statement: The data presented in this study are available within this article.

Conflicts of Interest: The authors declare no conflict of interest. The funders had no role in the design of the study; in the collection, analyses, or interpretation of data; in the writing of the manuscript; or in the decision to publish the results.

References

1. Nadeem, M.A.; Connelly, K.A.; Idriss, H. The photoreaction of TiO_2 and Au/TiO_2 single crystal and powder with organic adsorbates. *Int. J. Nanotechnol.* **2012**, *9*, 121–162. [CrossRef]
2. Li, L.; Hasan, I.M.U.; Farwa; He, R.; Peng, L.; Xu, N.; Niazi, N.K.; Zhang, J.-N.; Qiao, J. Copper as a single metal atom based photo-, electro-, and photoelectrochemical catalyst decorated on carbon nitride surface for efficient CO_2 reduction: A review. *Nano Res. Energy* **2022**, *1*, e9120015. [CrossRef]
3. Kudo, A.; Kato, H.; Tsuji, I. Strategies for the Development of Visible-light-driven Photocatalysts for Water Splitting. *Chem. Lett.* **2004**, *33*, 1534–1539. [CrossRef]
4. Maeda, K.; Kentaro, T.; Daling, L.; Tsuyoshi, T.; Nobuo, S.; Yasunobu, I.; Kazunari, D. Photocatalyst releasing hydrogen from water. *Nature* **2006**, *440*, 295. [CrossRef] [PubMed]
5. Kasahara, A.; Nukumizu, K.; Takata, T.; Kondo, J.N.; Hara, M.; Kobayashi, H.; Domen, K. $LaTiO_2N$ as a Visible-Light ($\leq$600 nm)-Driven Photocatalyst. *J. Phys. Chem. B* **2002**, *107*, 791–797. [CrossRef]
6. Cortright, R.D.; Davda, R.R.; Dumesic, J.A. Hydrogen from catalytic reforming of biomass-derived hydrocarbons in liquid water. *Nature* **2002**, *418*, 964–967. [CrossRef] [PubMed]
7. Deluga, G.A.; Salge, J.R.; Schmidt, L.D.; Verykios, X.E. Renewable Hydrogen from Ethanol by Autothermal Reforming. *Science* **2004**, *303*, 993–997. [CrossRef]
8. Holladay, J.D.; Hu, J.; King, D.L.; Wang, Y. An overview of hydrogen production technologies. *Catal. Today* **2009**, *139*, 244–260. [CrossRef]
9. Lewis, N.S.; Nocera, D.G. Powering the planet: Chemical challenges in solar energy utilization. *Proc. Natl. Acad. Sci. USA* **2006**, *103*, 15729–15735. [CrossRef]
10. Liu, Z.; Hou, W.; Pavaskar, P.; Aykol, M.; Cronin, S.B. Plasmon resonant enhancement of photocatalytic water splitting under visible illumination. *Nano Lett.* **2011**, *11*, 1111–1116. [CrossRef]
11. James, B.D.; Baum, G.N.; Perez, J.; Baum, K.N. Technoeconomic analysis of photoelectrochemical (PEC) hydrogen production. *DOE Rep.* **2009**.
12. Majeed, I.; Nadeem, M.A.; Hussain, E.; Waterhouse, G.I.; Badshah, A.; Iqbal, A.; Nadeem, M.A.; Idriss, H. On the synergism between Cu and Ni for photocatalytic hydrogen production and their potential as substitutes of noble metals. *ChemCatChem* **2016**, *8*, 3146–3155. [CrossRef]
13. Al-Azri, Z.H.N.; Chen, W.-T.; Chan, A.; Jovic, V.; Ina, T.; Idriss, H.; Waterhouse, G.I.N. The roles of metal co-catalysts and reaction media in photocatalytic hydrogen production: Performance evaluation of M/TiO_2 photocatalysts (M = Pd, Pt, Au) in different alcohol–water mixtures. *J. Catal.* **2015**, *329*, 355–367. [CrossRef]
14. Zhurenok, A.V.; Vasilchenko, D.B.; Kozlova, E.A. Comprehensive Review on g-C_3N_4-Based Photocatalysts for the Photocatalytic Hydrogen Production under Visible Light. *Int. J. Mol. Sci.* **2023**, *24*, 346. [CrossRef]
15. Rothenberger, G.; Moser, J.; Graetzel, M.; Serpone, N.; Sharma, D.K. Charge carrier trapping and recombination dynamics in small semiconductor particles. *J. Am. Chem. Soc.* **1985**, *107*, 8054–8059. [CrossRef]
16. Wad, A. Photocatalytic properties of TiO_2. *Chem. Mater.* **1993**, *5*, 280–283.
17. Fujishima, A.; Zhang, X.; Tryk, D.A. TiO_2 photocatalysis and related surface phenomena. *Surf. Sci. Rep.* **2008**, *63*, 515–582. [CrossRef]
18. Majeed, I.; Nadeem, M.A.; Kanodarwala, F.K.; Hussain, E.; Badshah, A.; Hussain, I.; Stride, J.A.; Nadeem, M.A. Controlled Synthesis of TiO_2 Nanostructures: Exceptional Hydrogen Production in Alcohol-Water Mixtures over $Cu(OH)_2$-Ni $(OH)_2/TiO_2$ Nanorods. *ChemistrySelect* **2017**, *2*, 7497–7507. [CrossRef]
19. Hong, Y.; Shi, P.; Wang, P.; Yao, W. Improved photocatalytic activity of CdS/reduced graphene oxide (RGO) for H_2 evolution by strengthening the connection between CdS and RGO sheets. *Int. J. Hydrog. Energy* **2015**, *40*, 7045–7051. [CrossRef]
20. Subramanian, V.; Wolf, E.E.; Kamat, P.V. Influence of Metal/Metal Ion Concentration on the Photocatalytic Activity of TiO_2-Au Composite Nanoparticles. *Langmuir* **2002**, *19*, 469–474. [CrossRef]

21. Muscetta, M.; Clarizia, L.; Garlisi, C.; Palmisano, G.; Marotta, R.; Andreozzi, R.; Di Somma, I. Hydrogen production upon UV-light irradiation of Cu/TiO$_2$ photocatalyst in the presence of alkanol-amines. *Int. J. Hydrog. Energy* **2020**, *45*, 26701–26715. [CrossRef]

22. Hoang, A.T.; Pandey, A.; Chen, W.-H.; Ahmed, S.F.; Nižetić, S.; Ng, K.H.; Said, Z.; Duong, X.Q.; Ağbulut, Ü.; Hadiyanto, H.; et al. Hydrogen Production by Water Splitting with Support of Metal and Carbon-Based Photocatalysts. *ACS Sustain. Chem. Eng.* **2023**, *11*, 1221–1252. [CrossRef]

23. Wu, C.; Guo, J.; Zhang, J.; Zhao, Y.; Tian, J.; Isimjan, T.T.; Yang, X. Palladium nanoclusters decorated partially decomposed porous ZIF-67 polyhedron with ultrahigh catalytic activity and stability on hydrogen generation. *Renew. Energy* **2019**, *136*, 1064–1070. [CrossRef]

24. Dai, Y.; Xiong, Y. Control of selectivity in organic synthesis via heterogeneous photocatalysis under visible light. *Nano Res. Energy* **2022**, *1*, 9120006. [CrossRef]

25. Fisher, A.; Peter, L.; Ponomarev, E.; Walker, A.; Wijayantha, K. Intensity dependence of the back reaction and transport of electrons in dye-sensitized nanocrystalline TiO$_2$ solar cells. *J. Phys. Chem. B* **2000**, *104*, 949–958. [CrossRef]

26. Yang, D.; Liu, H.; Zheng, Z.; Yuan, Y.; Zhao, J.-C.; Waclawik, E.R.; Ke, X.; Zhu, H. An efficient photocatalyst structure: TiO$_2$(B) nanofibers with a shell of anatase nanocrystals. *J. Am. Chem. Soc.* **2009**, *131*, 17885–17893. [CrossRef]

27. Sood, S.; Gouma, P. Polymorphism in nanocrystalline binary metal oxides. *Nanomater. Energy* **2013**, *2*, 82–96. [CrossRef]

28. Scanlon, D.O.; Dunnill, C.W.; Buckeridge, J.; Shevlin, S.A.; Logsdail, A.J.; Woodley, S.M.; Catlow, C.R.A.; Powell, M.J.; Palgrave, R.G.; Parkin, I.P. Band alignment of rutile and anatase TiO$_2$. *Nat. Mater.* **2013**, *12*, 798–801. [CrossRef] [PubMed]

29. Kumar, D.P.; Reddy, N.L.; Srinivas, B.; Durgakumari, V.; Roddatis, V.; Bondarchuk, O.; Karthik, M.; Ikuma, Y.; Shankar, M. Stable and active Cu$_x$O/TiO$_2$ nanostructured catalyst for proficient hydrogen production under solar light irradiation. *Sol. Energy Mater. Sol. Cells* **2016**, *146*, 63–71. [CrossRef]

30. Varghese, O.K.; Paulose, M.; Grimes, C.A. Long vertically aligned titania nanotubes on transparent conducting oxide for highly efficient solar cells. *Nat. Nanotechnol.* **2009**, *4*, 592–597. [CrossRef]

31. Chen, X.; Mao, S.S. Titanium dioxide nanomaterials: Synthesis, properties, modifications, and applications. *Chem. Rev.* **2007**, *107*, 2891–2959. [CrossRef]

32. Yoon, J.-W.; Sasaki, T.; Koshizaki, N. Dispersion of nanosized noble metals in TiO$_2$ matrix and their photoelectrode properties. *Thin Solid Film.* **2005**, *483*, 276–282. [CrossRef]

33. Ohtani, B.; Iwai, K.; Nishimoto, S.-I.; Sato, S. Role of Platinum Deposits on Titanium (IV) Oxide Particles: Structural and Kinetic Analyses of Photocatalytic Reaction in Aqueous Alcohol and Amino Acid Solutions. *J. Phys. Chem. B* **1997**, *101*, 3349–3359. [CrossRef]

34. Kamat, P.V. Photophysical, Photochemical and Photocatalytic Aspects of Metal Nanoparticles. *J. Phys. Chem. B* **2002**, *106*, 7729–7744. [CrossRef]

35. Lee, S.; Scott, J.; Chiang, K.; Amal, R. Nanosized metal deposits on titanium dioxide for augmenting gas-phase toluene photooxidation. *J. Nanopart. Res.* **2009**, *11*, 209–219. [CrossRef]

36. Hoffmann, M.R.; Martin, S.T.; Choi, W.; Bahnemann, D.W. Environmental applications of semiconductor photocatalysis. *Chem. Rev.* **1995**, *95*, 69–96. [CrossRef]

37. Linsebigler, A.L.; Lu, G.; Yates, J.T., Jr. Photocatalysis on TiO$_2$ surfaces: Principles, mechanisms, and selected results. *Chem. Rev.* **1995**, *95*, 735–758. [CrossRef]

38. Tabata, S.; Nishida, H.; Masaki, Y.; Tabata, K. Stoichiometric photocatalytic decomposition of pure water in Pt/TiO$_2$ aqueous suspension system. *Catal. Lett.* **1995**, *34*, 245–249. [CrossRef]

39. Sato, S.; White, J. Photodecomposition of water over Pt/TiO$_2$ catalysts. *Chem. Phys. Lett.* **1980**, *72*, 83–86. [CrossRef]

40. Haruta, M. Size- and support-dependency in the catalysis of gold. *Catal. Today* **1997**, *36*, 153–166. [CrossRef]

41. Tian, H.; Kang, S.-Z.; Li, X.; Qin, L.; Ji, M.; Mu, J. Fabrication of an efficient noble metal-free TiO$_2$-based photocatalytic system using Cu–Ni bimetallic deposit as an active center of H$_2$ evolution from water. *Sol. Energy Mater. Sol. Cells* **2015**, *134*, 309–317. [CrossRef]

42. Majeed, I.; Nadeem, M.A.; Badshah, A.; Kanodarwala, F.K.; Ali, H.; Khan, M.A.; Stride, J.A.; Nadeem, M.A. Titania supported MOF-199 derived Cu-Cu$_2$O nanoparticles: Highly efficient non-noble metal photocatalysts for hydrogen production from alcohol–water mixtures. *Catal. Sci. Technol.* **2017**, *7*, 677–686. [CrossRef]

43. Chen, W.-T.; Chan, A.; Sun-Waterhouse, D.; Moriga, T.; Idriss, H.; Waterhouse, G.I. Ni/TiO$_2$: A promising low-cost photocatalytic system for solar H$_2$ production from ethanol–water mixtures. *J. Catal.* **2015**, *326*, 43–53. [CrossRef]

44. Majeed, I.; Arif, A.; Faizan, M.; Khan, M.A.; Imran, M.; Ali, H.; Nadeem, M.A.; Nadeem, M.A. CdS nanorods supported copper-nickel hydroxide for hydrogen production under direct sunlight irradiation. *J. Environ. Chem. Eng.* **2021**, *9*, 105670. [CrossRef]

45. Yu, J.; Ran, J. Facile preparation and enhanced photocatalytic H$_2$-production activity of Cu(OH)$_2$ cluster modified TiO$_2$. *Energy Environ. Sci.* **2011**, *4*, 1364–1371. [CrossRef]

46. Ismail, A.A.; Al-Sayari, S.A.; Bahnemann, D. Photodeposition of precious metals onto mesoporous TiO$_2$ nanocrystals with enhanced their photocatalytic activity for methanol oxidation. *Catal. Today* **2013**, *209*, 2–7. [CrossRef]

47. Bowker, M.; Morton, C.; Kennedy, J.; Bahruji, H.; Greves, J.; Jones, W.; Davies, P.R.; Brookes, C.; Wells, P.; Dimitratos, N. Hydrogen production by photoreforming of biofuels using Au, Pd and Au-Pd/TiO$_2$ photocatalysts. *J. Catal.* **2014**, *310*, 10–15. [CrossRef]

48. Majeed, I.; Manzoor, U.; Kanodarwala, F.K.; Nadeem, M.A.; Hussain, E.; Ali, H.; Badshah, A.; Stride, J.A.; Nadeem, M.A. Pd–Ag decorated gC$_3$N$_4$ as an efficient photocatalyst for hydrogen production from water under direct solar light irradiation. *Catal. Sci. Technol.* **2018**, *8*, 1183–1193. [CrossRef]

49. Hussain, E.; Majeed, I.; Nadeem, M.A.; Badshah, A.; Chen, Y.; Nadeem, M.A.; Jin, R. Titania-supported palladium/strontium nanoparticles (Pd/Sr-NPs@ P25) for photocatalytic H$_2$ production from water splitting. *J. Phys. Chem. C* **2016**, *120*, 17205–17213. [CrossRef]

50. Majeed, I.; Ali, H.; Idrees, A.; Arif, A.; Ashraf, W.; Rasul, S.; Khan, M.A.; Nadeem, M.A.; Nadeem, M.A. Understanding the role of metal supported on TiO$_2$ in photoreforming of oxygenates. *Energy Adv.* **2022**, *1*, 842–867. [CrossRef]

51. Ali, H.; Kanodarwala, F.K.; Majeed, I.; Stride, J.A.; Nadeem, M.A. La$_2$O$_3$ Promoted Pd/rGO electro-catalysts for formic acid oxidation. *ACS Appl. Mater. Interfaces* **2016**, *8*, 32581–32590. [CrossRef]

52. Nishimura, S. *Handbook of Heterogeneous Catalytic Hydrogenation for Organic Synthesis*; Wiley: New York, NY, USA, 2001.

53. Hussain, E.; Majeed, I.; Nadeem, M.A.; Iqbal, A.; Chen, Y.; Choucair, M.; Jin, R.; Nadeem, M.A. Remarkable effect of BaO on photocatalytic H$_2$ evolution from water splitting via TiO$_2$ (P25) supported palladium nanoparticles. *J. Environ. Chem. Eng.* **2019**, *7*, 102729. [CrossRef]

54. Dosado, A.G.; Chen, W.-T.; Chan, A.; Sun-Waterhouse, D.; Waterhouse, G.I.N. Novel Au/TiO$_2$ photocatalysts for hydrogen production in alcohol-water mixtures based on hydrogen titanate nanotube precursors. *J. Catal.* **2015**, *330*, 238–254. [CrossRef]

55. Stankovich, S.; Dikin, D.A.; Piner, R.D.; Kohlhaas, K.A.; Kleinhammes, A.; Jia, Y.; Wu, Y.; Nguyen, S.T.; Ruoff, R.S. Synthesis of graphene-based nanosheets via chemical reduction of exfoliated graphite oxide. *Carbon* **2007**, *45*, 1558–1565. [CrossRef]

56. Majeed, I.; Nadeem, M.A.; Hussain, E.; Badshah, A.; Gilani, R.; Nadeem, M.A. Effect of deposition method on metal loading and photocatalytic activity of Au/CdS for hydrogen production in water electrolyte mixture. *Int. J. Hydrog. Energy* **2017**, *42*, 3006–3018. [CrossRef]

57. Nadeem, A.; Muir, J.; Connelly, K.; Adamson, B.; Metson, B.; Idriss, H. Ethanol photo-oxidation on a rutile TiO$_2$ (110) single crystal surface. *Phys. Chem. Chem. Phys.* **2011**, *13*, 7637–7643. [CrossRef]

58. Majeed, I.; Nadeem, M.A.; Al-Oufi, M.; Nadeem, M.A.; Waterhouse, G.I.N.; Badshah, A.; Metson, J.B.; Idriss, H. On the role of metal particle size and surface coverage for photo-catalytic hydrogen production: A case study of the Au/CdS system. *Appl. Catal. B Environ.* **2016**, *182*, 266–276. [CrossRef]

59. Dou, S.; Zhou, S.; Huang, H.; Yan, P.; Shoko, E.; Isimjan, T.T.; Yang, X. Metal—Organic Framework (MOF)-Derived Electron-Transfer Enhanced Homogeneous PdO-Rich Co$_3$O$_4$ as a Highly Efficient Bifunctional Catalyst for Sodium Borohydride Hydrolysis and 4-Nitrophenol Reduction. *Chem.-A Eur. J.* **2020**, *26*, 16923–16931. [CrossRef] [PubMed]

60. Fan, W.; Lai, Q.; Zhang, Q.; Wang, Y. Nanocomposites of TiO$_2$ and reduced graphene oxide as efficient photocatalysts for hydrogen evolution. *J. Phys. Chem. C* **2011**, *115*, 10694–10701. [CrossRef]

61. Sheha, E. Studies on TiO$_2$/reduced graphene oxide composites as cathode materials for magnesium-ion battery. *Graphene* **2014**, *2014*, 48098. [CrossRef]

62. Cataldo, F.; Ursini, O.; Angelini, G. Graphite oxide and graphene nanoribbons reduction with hydrogen iodide. *Fuller. Nanotub. Carbon Nanostructures* **2011**, *19*, 461–468. [CrossRef]

63. Hodkiewicz, J.; Scientific, T. Characterizing carbon materials with Raman spectroscopy. *Sci. Appl. Note* **2010**, *51946*.

64. Yang, D.; Velamakanni, A.; Bozoklu, G.; Park, S.; Stoller, M.; Piner, R.D.; Stankovich, S.; Jung, I.; Field, D.A.; Ventrice, C.A., Jr. Chemical analysis of graphene oxide films after heat and chemical treatments by X-ray photoelectron and Micro-Raman spectroscopy. *Carbon* **2009**, *47*, 145–152. [CrossRef]

65. Ali, H.; Zaman, S.; Majeed, I.; Kanodarwala, F.K.; Nadeem, M.A.; Stride, J.A.; Nadeem, M.A. Porous Carbon/rGO Composite: An Ideal Support Material of Highly Efficient Palladium Electrocatalysts for the Formic Acid Oxidation Reaction. *ChemElectroChem* **2017**, *4*, 3126–3133. [CrossRef]

66. Johra, F.T.; Lee, J.-W.; Jung, W.-G. Facile and safe graphene preparation on solution based platform. *J. Ind. Eng. Chem.* **2014**, *20*, 2883–2887. [CrossRef]

67. Nadeem, M.A.; Al-Oufi, M.; Wahab, A.K.; Anjum, D.; Idriss, H. Hydrogen Production on Ag-Pd/TiO$_2$ Bimetallic Catalysts: Is there a Combined Effect of Surface Plasmon Resonance with Schottky Mechanism on the Photo-Catalytic Activity? *ChemistrySelect* **2017**, *2*, 2754–2762. [CrossRef]

68. Nadeem, M.A.; Waterhouse, G.I.N.; Idriss, H. A study of ethanol reactions on O$_2$-treated Au/TiO$_2$. Effect of support and metal loading on reaction selectivity. *Surf. Sci.* **2016**, *650*, 40–50. [CrossRef]

69. Xiang, Q.; Yu, J.; Jaroniec, M. Synergetic effect of MoS$_2$ and graphene as cocatalysts for enhanced photocatalytic H$_2$ production activity of TiO$_2$ nanoparticles. *J. Am. Chem. Soc.* **2012**, *134*, 6575–6578. [CrossRef] [PubMed]

70. Naldoni, A.; D'Arienzo, M.; Altomare, M.; Marelli, M.; Scotti, R.; Morazzoni, F.; Selli, E.; Dal Santo, V. Pt and Au/TiO$_2$ photocatalysts for methanol reforming: Role of metal nanoparticles in tuning charge trapping properties and photoefficiency. *Appl. Catal. B Environ.* **2013**, *130*, 239–248. [CrossRef]

71. Zhu, G.; Su, F.; Lv, T.; Pan, L.; Sun, Z. Au nanoparticles as interfacial layer for CdS quantum dot-sensitized solar cells. *Nanoscale Res. Lett.* **2010**, *5*, 1749–1754. [CrossRef] [PubMed]

72. Su, R.; Tiruvalam, R.; Logsdail, A.J.; He, Q.; Downing, C.A.; Jensen, M.T.; Dimitratos, N.; Kesavan, L.; Wells, P.P.; Bechstein, R. Designer titania-supported Au-Pd nanoparticles for efficient photocatalytic hydrogen production. *ACS Nano* **2014**, *8*, 3490–3497. [CrossRef]

73. Cheng, P.; Yang, Z.; Wang, H.; Cheng, W.; Chen, M.; Shangguan, W.; Ding, G. TiO$_2$—Graphene nanocomposites for photocatalytic hydrogen production from splitting water. *Int. J. Hydrog. Energy* **2012**, *37*, 2224–2230. [CrossRef]

74. Xiang, Q.; Yu, J.; Jaroniec, M. Enhanced photocatalytic H$_2$-production activity of graphene-modified titania nanosheets. *Nanoscale* **2011**, *3*, 3670–3678. [CrossRef]

75. Zhang, X.; Sun, Y.; Cui, X.; Jiang, Z. A green and facile synthesis of TiO$_2$/graphene nanocomposites and their photocatalytic activity for hydrogen evolution. *Int. J. Hydrog. Energy* **2012**, *37*, 811–815. [CrossRef]

76. Zhang, X.-Y.; Li, H.-P.; Cui, X.-L.; Lin, Y. Graphene/TiO$_2$ nanocomposites: Synthesis, characterization and application in hydrogen evolution from water photocatalytic splitting. *J. Mater. Chem.* **2010**, *20*, 2801–2806. [CrossRef]

77. Kim, H.-I.; Moon, G.-H.; Monllor-Satoca, D.; Park, Y.; Choi, W. Solar photoconversion using graphene/TiO$_2$ composites: Nanographene shell on TiO$_2$ core versus TiO$_2$ nanoparticles on graphene sheet. *J. Phys. Chem. C* **2012**, *116*, 1535–1543. [CrossRef]

78. Wang, B.; Sun, Q.; Liu, S.; Li, Y. Synergetic catalysis of CuO and graphene additives on TiO$_2$ for photocatalytic water splitting. *Int. J. Hydrog. Energy* **2013**, *38*, 7232–7240. [CrossRef]

79. Chen, W.-T.; Jovic, V.; Sun-Waterhouse, D.; Idriss, H.; Waterhouse, G.I.N. The role of CuO in promoting photocatalytic hydrogen production over TiO$_2$. *Int. J. Hydrog. Energy* **2013**, *38*, 15036–15048. [CrossRef]

80. Yu, J.; Hai, Y.; Cheng, B. Enhanced photocatalytic H$_2$-production activity of TiO$_2$ by Ni(OH)$_2$ cluster modification. *J. Phys. Chem. C* **2011**, *115*, 4953–4958. [CrossRef]

81. Rayalu, S.S.; Jose, D.; Joshi, M.V.; Mangrulkar, P.A.; Shrestha, K.; Klabunde, K. Photocatalytic water splitting on Au/TiO$_2$ nanocomposites synthesized through various routes: Enhancement in photocatalytic activity due to SPR effect. *Appl. Catal. B Environ.* **2013**, *142–143*, 684–693. [CrossRef]

82. Ortega Méndez, J.A.; López, C.R.; Pulido Melián, E.; González Díaz, O.; Doña Rodríguez, J.M.; Fernández Hevia, D.; Macías, M. Production of hydrogen by water photo-splitting over commercial and synthesised Au/TiO$_2$ catalysts. *Appl. Catal. B Environ.* **2014**, *147*, 439–452. [CrossRef]

83. Chiarello, G.L.; Selli, E.; Forni, L. Photocatalytic hydrogen production over flame spray pyrolysis-synthesised TiO$_2$ and Au/TiO$_2$. *Appl. Catal. B Environ.* **2008**, *84*, 332–339. [CrossRef]

84. Gärtner, F.; Losse, S.; Boddien, A.; Pohl, M.M.; Denurra, S.; Junge, H.; Beller, M. Hydrogen evolution from water/alcohol mixtures: Effective in situ generation of an active Au/TiO$_2$ catalyst. *ChemSusChem* **2012**, *5*, 530–533. [CrossRef]

85. Gallo, A.; Marelli, M.; Psaro, R.; Gombac, V.; Montini, T.; Fornasiero, P.; Pievo, R.; Dal Santo, V. Bimetallic Au-Pt/TiO$_2$ photocatalysts active under UV-A and simulated sunlight for H$_2$ production from ethanol. *Green Chem.* **2012**, *14*, 330–333. [CrossRef]

86. Wu, M.-C.; Lee, P.-H.; Lee, D.-L. Enhanced photocatalytic activity of palladium decorated TiO$_2$ nanofibers containing anatase-rutile mixed phase. *Int. J. Hydrog. Energy* **2015**, *40*, 4558–4566. [CrossRef]

87. Fujita, S.-I.; Kawamori, H.; Honda, D.; Yoshida, H.; Arai, M. Photocatalytic hydrogen production from aqueous glycerol solution using NiO/TiO$_2$ catalysts: Effects of preparation and reaction conditions. *Appl. Catal. B Environ.* **2016**, *181*, 818–824. [CrossRef]

88. Agegnehu, A.K.; Pan, C.-J.; Rick, J.; Lee, J.-F.; Su, W.-N.; Hwang, B.-J. Enhanced hydrogen generation by cocatalytic Ni and NiO nanoparticles loaded on graphene oxide sheets. *J. Mater. Chem.* **2012**, *22*, 13849–13854. [CrossRef]